Reverse Recovery Optimization of Multiepi Superjunction MOSFET Based on Tunable Doping Profile

Liu, Ke ; Tan, Chunjian; Li, Shizhen; Yuan, Wucheng ; Liu, Xu; Zhang, Guoqi; French, Paddy; Ye, Huaiyu ; Wang, Shaogang

DOI
10.3390/electronics12132977

Publication date
2023

Document Version
Final published version

Published in
Electronics (Switzerland)

electronics

MDPI

Article

Reverse Recovery Optimization of Multiepi Superjunction MOSFET Based on Tunable Doping Profile

Ke Liu [1], Chunjian Tan [1,2], Shizhen Li [1], Wucheng Yuan [1], Xu Liu [1,2], Guoqi Zhang [2], Paddy French [2], Huaiyu Ye [1,2,*] and Shaogang Wang [1,2,*]

[1] School of Microelectronics, Southern University of Science and Technology, Shenzhen 518055, China; 12132459@mail.sustech.edu.cn (K.L.); c.tan@tudelft.nl (C.T.); lisz@mail.sustech.edu.cn (S.L.); 12132485@mail.sustech.edu.cn (W.Y.); liux32019@mail.sustech.edu.cn (X.L.)

[2] Faculty of EEMCS, Delft University of Technology, Mekelweg 4, 2628 CD Delft, The Netherlands; g.q.zhang@tudelft.nl (G.Z.); p.j.french@tudelft.nl (P.F.)

* Correspondence: yehy@sustech.edu.cn (H.Y.); s.wang-10@tudelft.nl (S.W.)

Abstract: This paper proposes and simulates research on the reverse recovery characteristics of two novel superjunction (SJ) MOSFETs by adjusting the doping profile. In the manufacturing process of the SJ MOSFET using multilayer epitaxial deposition (MED), the position and concentration of each Boron bubble can be adjusted by designing different doping profiles to adjust the resistance of the upper half P-pillar. A higher P-pillar resistance can slow down the sweep out speed of hole carriers when the body diode is turned off, thus resulting in a smoother reverse recovery current and reducing the current recovery rate (d_{ir}/d_t) from a peak to zero. The simulation results show that the reverse recovery peak current (I_{rrm}) of the two proposed devices decreased by 5% and 3%, respectively, compared to the conventional SJ. Additionally, the softness factor (S) increased by 64% and 55%, respectively. Furthermore, this study also demonstrates a trade-off relationship between static and reverse recovery characteristics with the adjustable doping profile, thus providing a guideline for actual application scenarios.

Keywords: superjunction; MOSFET; doping profile; reverse recovery; body diode

Citation: Liu, K.; Tan, C.; Li, S.; Yuan, W.; Liu, X.; Zhang, G.; French, P.; Ye, H.; Wang, S. Reverse Recovery Optimization of Multiepi Superjunction MOSFET Based on Tunable Doping Profile. *Electronics* **2023**, *12*, 2977. https://doi.org/10.3390/electronics12132977

Academic Editor: Ahmed Abu-Siada

Received: 1 June 2023
Revised: 23 June 2023
Accepted: 4 July 2023
Published: 6 July 2023

1. Introduction

The superjunction (SJ) MOSFET finds extensive use in white goods within the range of 500–900 V due to it breaking the silicon limit, thus resulting in a lower special on-resistance ($R_{on,sp}$) compared to conventional MOSFETs with the same breakdown voltage (BV) requirements [1,2]. However, due to its unique drift region structure, the SJ MOSFET not only has a complicated manufacturing process, but also exhibits a poor reverse recovery characteristic when its body diode acts as a freewheeling diode in the soft switching circuit [3]. The large amount of the nonequilibrium carriers' stored charge (Q_{rr}) and the extremely fast reverse recovery current change rate (d_i/d_t) limit the application of the SJ MOSFET in high-frequency inductive circuits [4]. Moreover, the trench etch backfilling (TEB) and multilayer epitaxial deposition (MED) are two commonly used processes for fabricating the pillar region of the SJ MOSFET [5,6]. The TEB process can build a more uniform N/P-pillar morphology, which realizes a better trade-off between the BV and $R_{on,sp}$ of the SJ MOSFET [7]. By contrast, the MED process allows for greater flexibility in constructing the vertical doping profile during device fabrication [8]. In the details of the MED process, the doping profile can be precisely controlled by adjusting the energy, concentration, and ion implantation position in multiple steps [9]. Therefore, derived vertical variable doping (VVD) technology enables the fabrication of SJ MOSFETs with different doping profiles in the pillar region. Compared to conventional SJ devices with a uniform doping profile, VVD technology not only enhances the BV window of superjunction devices, but also further reduces the $R_{on,sp}$ during the conduction period [10].

Previous research has demonstrated that the P-pillar formed with a high-k insulator material reduces Q_{rr} storage while optimizing the charge balance in the SJ MOSFET [11]. Moreover, in the SJ MOSFET fabricated with the MED process, increasing the resistance of the P-pillar can effectively suppress the current oscillation during reverse recovery [12]. Furthermore, our previous research work has also indicated that adjusting the P-pillar resistance of the SJ MOSFET can help improve the softness factor (S) of the body diode during reverse recovery [13]. In this paper, we proposed two new methods to increase the local resistance of the P-pillar by adjusting the vertical doping profile in the pillar region. The first method focuses on a horizontal adjustment of the Boron ion implantation windows, thereby allowing a precise control over implantation positions, and the second method involves a vertical adjustment of the Boron ion concentration within the P/N-pillar. Importantly, these adjustments are made without modifying the total implantation concentration of the P/N-pillar to ensure the form of the desired doping profile. Notably, both approaches are rooted in the MED process, thus leveraging its capabilities for precise control and optimization.

The paper is structured as follows. In Section 2, two vertical doping profile design schemes in the pillar region are proposed. Section 3 presents the simulation experiment schemes, including the experimental results and mechanisms analysis. Finally, the conclusions are summarized in Section 4. The TCAD tool was utilized for model construction and simulation analysis, which incorporates carrier mobility models (Doping Dependence and High Field Saturation), recombination models (Shockley Read Hall and Auger), and effective intrinsic density model (OldSlotboom).

2. Device Structure and Mechanism

This section focuses on the utilization of TCAD tools to construct simulation models of the superjunction MOSFET through the MED process. Two variations of the superjunction MOSFET with novel doping profiles were designed and simulated. Additionally, design of experiment (DOE) experiments were conducted to explore the impact of doping profile variations on the device electrical performance. These experiments aim to investigate the relationship between different doping profile parameters and the resulting electrical characteristics of the device.

Figure 1a shows the cell cross-sectional diagrams of the conventional SJ MOSFET (Conv-SJ) based on the MED process. The pillar region is constructed through multiple alternating processes of N-type epitaxy and Boron ion implantation. In the Conv-SJ, the doping profile of the P-pillar features straight-line ion implantation windows with a consistent implantation concentration at each implantation step. Then, in Figure 1b, a bubble shift SJ MOSFET (BS-SJ) with a novel doping profile is proposed. The N-type epitaxy and Boron bubble implantation strategy in the bottom half of the pillar region is the same as that in the Conv-SJ, but the last several Boron implantation windows in the top half of the P-pillar are shifted alternately from left to right along the center of the cell. Additionally, Figure 1c proposes another concentration shift SJ MOSFET (CS-SJ) with a novel doping profile in which the Boron ion implantation concentration of the P-pillar is divided into three sections. The concentration in the middle part of the pillar region is consistent with the Conv-SJ, while the implantation concentration in the upper and lower parts is designed to be shifted. Compared with the middle part, the upper part of the P-pillar has a lower implantation concentration, and the lower part has a higher implantation concentration, but the sum of the P-pillar concentrations is equal to that of the Conv-SJ. Table 1 displays the key parameters of the SJ MOSFET cell simulation model.

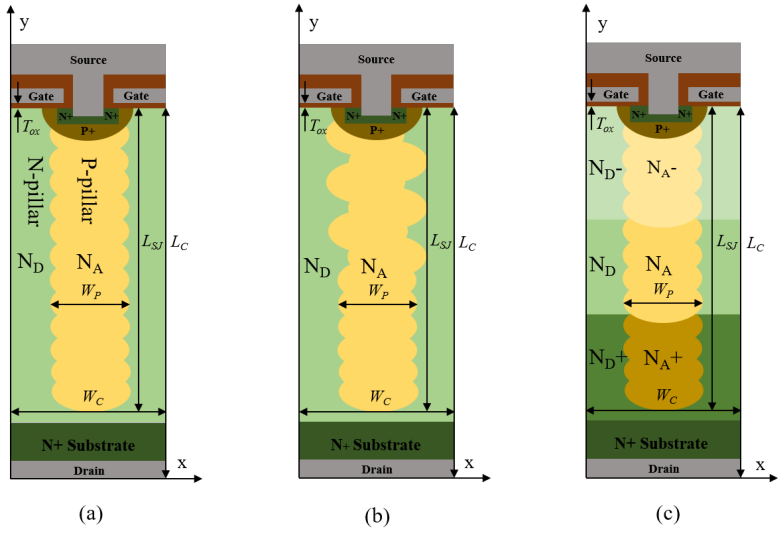

Figure 1. The cell cross-sectional of (**a**) conventional SJ MOSFET, (**b**) bubble shift SJ MOSFET, and (**c**) concentration shift SJ MOSFET.

Table 1. Key cell structure simulation parameters.

Symbol	Definition	Value
W_c	Cell Pitch	5.5 µm
W_p	P-pillar Width	2.5 µm
L_{SJ}	SJ Layer Length	42 µm
L_c	Cell Length	53 µm
T_{ox}	Gate Oxide Thickness	0.1 µm
N_D	Donor Concentration	1×10^{16} cm^{-3}
N_A	Acceptor Concentration	1×10^{16} cm^{-3}

Figure 2 shows the net charge distribution of the Conv-SJ, BS-SJ, and CS-SJ in the P-pillar after annealing. It is evident that the tunable doping profile primarily changes the P-pillar morphology and Boron concentration distributions. In the P-pillar of the BS-SJ, the net charge concentration in the top half is lower than that of the Conv-SJ, and the net charge concentration in the bottom half is almost the same as that of the Conv-SJ. This is because, after annealing, the peak value of the concentration Gaussian distribution of the Boron bubbles in the top half of the P-pillar is not aligned on the same straight line. Meanwhile, the formed bent section relatively extends the length of the P-pillar, which prolongs the hole carrier sweep out path and reduces the net charge concentration in the bent areas. In contrast, the CS-SJ modifies the net charge concentration distribution in the P-pillar directly. For this condition, the doping profile of the middle part of the P-pillar is identical to that of the Conv-SJ, while the upper and lower parts exhibit a concentration difference. Since the charge balance in the SJ layer is highly sensitive, the same concentration shift is necessary in the N-pillar of the CS-SJ.

From the above observations, it can be inferred that the two methods of adjusting the doping profile will directly result in an increase in the local resistance of the P-pillar. This, in turn, has an impact on the process of the sweep out for stored non-equilibrium minority carriers in the P/N-pillar region during the reverse recovery. To further investigate the influence of the doping profile shift degree on the electrical performance of the SJ MOSFETs, the shift degree was divided into 8 levels in Table 2. Among them, the shift level 1 represents the doping profile of the Conv-SJ. Furthermore, to explore the interaction between the two methods of adjusting the doping profile, the superposition effect of the bubble and concentration shift SJ MOSFET (BCS-SJ) was also simulated and discussed.

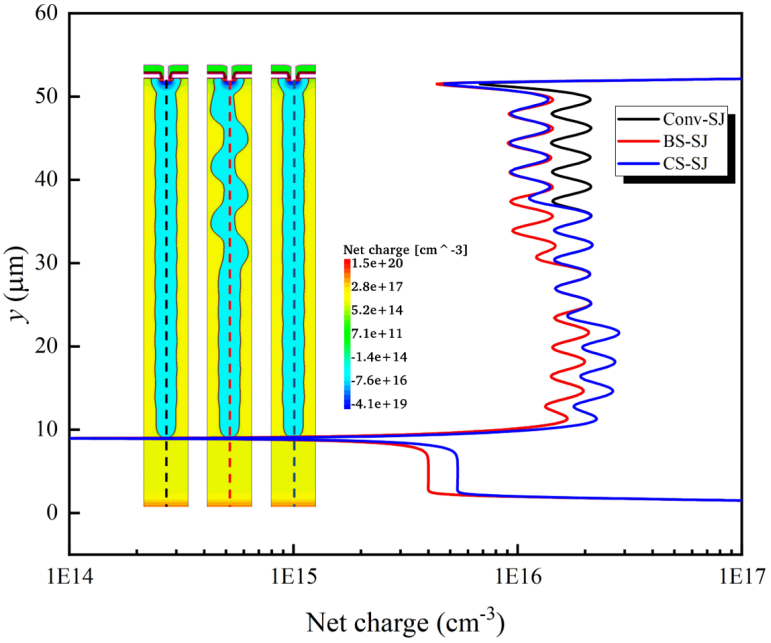

Figure 2. The net charge distribution of the three devices along the center (x = 2.75 μm) of the P−pillar.

Table 2. Design scheme of simulation experiment.

Shift Level	Bubble Shift	Concentration Shift	Bubble and Concentration Shift
1	-	-	-
2	0.1 μm	5%	0.1 μm and 5%
3	0.2 μm	10%	0.2 μm and 10%
4	0.3 μm	15%	0.3 μm and 15%
5	0.4 μm	20%	0.4 μm and 20%
6	0.5 μm	25%	0.5 μm and 25%
7	0.6 μm	30%	0.6 μm and 30%
8	0.7 μm	35%	0.7 μm and 35%

3. Simulation Results and Analysis

In this section, the focus of the research is to elucidate the adjustment trends of the two novel doping profiles on the static characteristics of the SJ MOSFET. Additionally, a comprehensive analysis was conducted from the perspective of carriers behavior to investigate the physical mechanisms underlying the improvement of the diode reverse recovery characteristics in the SJ MOSFET with the two novel doping profiles. Throughout this analysis, particular attention was given to the correlation between the improvement methods of the two novel doping profiles and the device electrical performance. Finally, a comprehensive approach for evaluating the trade-off between the static and dynamic characteristics of the SJ MOSFET was obtained.

Figure 3a shows the blocking characteristics of the three devices. The drain-source breakdown voltage (BV) of the BS-SJ with a 0.4 μm bubble shift and CS-SJ with a 20% concentration shift was slightly lower than that of the Conv-SJ. This is because of the redistribution of the transverse charge field of the SJ MOSFET caused by the bubble shift and concentration shift. The redistribution phenomenon caused the charge field to accumulate in a localized area at the junction interface between the N-pillar and P-pillar, thus ultimately resulting in an increase in the peak value of the electric field and a reduction in the withstand voltage capacity of the SJ MOSFET.

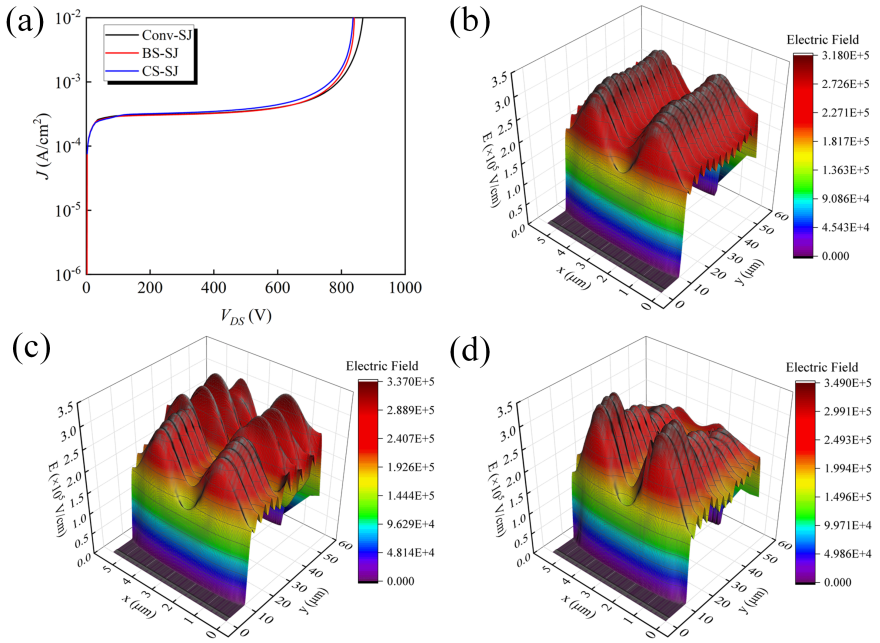

Figure 3. (**a**) The blocking characteristics of the three devices at 300 K. (**b**) The electric field distribution when the conventional SJ MOSFET is blocked. (**c**) The electric field distribution when the bubble shift SJ MOSFET is blocked. (**d**) The electric field distribution when the concentration shift SJ MOSFET is blocked.

Figure 3b illustrates that the electric field of the Conv-SJ was primarily composed of the longitudinal potential field and the transverse charge field [14]. The electric field, which was constructed by the doping profile without a shift, was uniform and straight along the longitudinal distribution, and its peak value was 3.18×10^5 V/cm. As depicted in Figure 3c, the electric field distribution in the P/N-pillar region of the BS-SJ, where the doping profile was the same, was consistent with that of the Conv-SJ. However, the electric field of the bubble shift parts also shifted along the longitudinal direction. This phenomenon worsened the uniformity of the longitudinal potential field while causing the transverse charge field to become more concentrated at the bending parts. This, in turn, increased the peak electric field (3.37×10^5 V/cm) and decreased the withstand capability of the BS-SJ. Meanwhile, in Figure 3d, the electric field distribution of the CS-SJ also exhibited a three-segment distribution due to concentration shift. Since the peak value of the charge field was positively correlated with the carrier concentration, a higher concentration doping profile at the bottom of the CS-SJ also increased the peak electric field (3.49×10^5 V/cm), which led to avalanche breakdown in advance.

Figure 4 shows the impact of the shift level on the BV and $R_{on,sp}$ of the BS-SJ and CS-SJ, respectively. Before adjusting the doping profile, the BV and $R_{on,sp}$ of the Conv-SJ were 705 V and 9.8 m$\Omega \cdot$ cm^{-3}, respectively. After modifying the doping profile of the pillar region by using two different methods, both the BS-SJ and CS-SJ exhibited a continuous decrease in the BV and a continuous increase in the $R_{on,sp}$ with the shift level increases. Compared to the Conv-SJ, in the BS-SJ, the BV at shift level 8 was 692 V, which only decreased by 2%. However, in the CS-SJ, the BV was more significantly affected by the shift level, and the BV dropped sharply after a 20% concentration shift to reach a withstand voltage value of 534 V at shift level 8 ultimately, thus resulting in a 24% decrease in the BV. This is because the peak value of the charge field increased with the shift level increase in the SJ MOSFET withstand voltage field, and the charge field was more sensitive with the changes in doping concentration. Similarly, compared to the Conv-SJ, in the BS -SJ, the $R_{on,sp}$ at shift level 8 was 12.4 m$\Omega \cdot$ cm^{-3}, which increased by 26%. In the CS-SJ, the $R_{on,sp}$ at shift level 8 was 12.7 m$\Omega \cdot$ cm^{-3}, which represents a 29% increase. This is because the

curved part of the P-pillar narrowed the conduction path for electronics in the BS-SJ, thus increasing the conduction resistance when the BS-SJ was in the on state. Meanwhile, the charge balance needed to be maintained in the upper part of the P/N-pillar in the CS-SJ. The doping concentration in the N-pillar also needed to decrease in accordance with the doping profile of the P-pillar, thus resulting in an increase in the $R_{on,sp}$ as well.

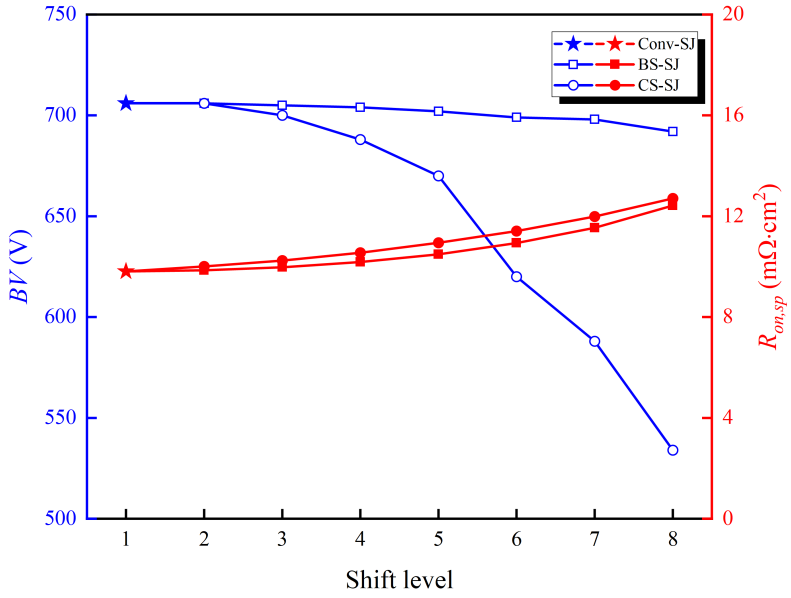

Figure 4. The influence of the shift level on the breakdown voltage BV and special on-resistance $R_{on,sp}$.

Owing to the hole mobility being smaller than the electron mobility in silicon, the reverse recovery performance of the body diode was mainly determined by hole carriers. Figure 5 depicts the hole current density of the Conv-SJ, 0.7 µm of the BS-SJ, and 35% of the CS-SJ during the reverse recovery phase under forward-bias conditions of the body diode. In the BS-SJ, the hole current density in the upper half of the P-pillar was significantly lower than that in the Conv-SJ, while the hole current in the lower half was almost the same. This difference arose from the increased length of the P-pillar bending region, which led to a lower Boron concentration in this area after annealing compared with the Conv-SJ, while the overall Boron doping concentration remained unchanged, thus resulting in a reduced induced hole current density in this region. In the CS-SJ, the hole current density in the upper part of the P-pillar was lower than that in the Conv-SJ. In the middle section, it remained consistent, while, in the lower part, it was higher. This phenomenon is caused by the varying local resistance values of the P-pillar, which is attributed to the three-segment doping profile of the Boron concentration. By these two ways, the resistance of the upper part of the P-pillar in the BS-SJ and CS-SJ was higher than that in the Conv-SJ, which can increase the resistance of the hole extraction path during the reverse recovery [15].

Figure 6 depicts the hole density of the Conv-SJ, BS-SJ, and CS-SJ at the different time nodes during the carrier extraction stage of reverse recovery. At 8 ns, the PN junction, which is formed by the P-pillar and N-pillar, began to withstand bias voltage. Under the influence of the electric field, the depletion region constructed from the upper portion of the P-base/N-pillar and extended towards the bottom along the P/N-pillar. Meanwhile, the stored hole carriers and electron carriers in the drift region began to sweep out. At 12 ns, the hole carriers in the top half of the N-pillar region had been nearly removed in all three devices. Following this, the hole carriers in the lower half of the N-pillar region continued to be swept out through the conduction path of the P-pillar, at which time the distribution of the remaining hole carriers in the three devices began to differ. At 16 ns, the remaining hole carriers in the drift region of the Conv-SJ device were rapidly and completely extracted due to the uniform and straight doping profile of the P-pillar. By contrast, the BS-SJ exhibited a

longer hole sweep path due to the bubble shift and an increased resistance in the P-pillar due to the bending, thus resulting in a slower carrier sweep out speed. Similarly, the CS-SJ exhibited higher resistance due to a lower Boron doping concentration in the upper part of the P-pillar, thus leading to a decrease in hole carrier sweep out speed. On the other hand, the higher doping concentration in the lower part of the P-pillar enabled more residual hole carriers to smooth the reverse recovery current. At 20 ns, it was evident that a significant number of residual hole carriers were waiting to be swept out through the P-pillar path at the bottom in both the BS-SJ and CS-SJ when compared to the Conv-SJ.

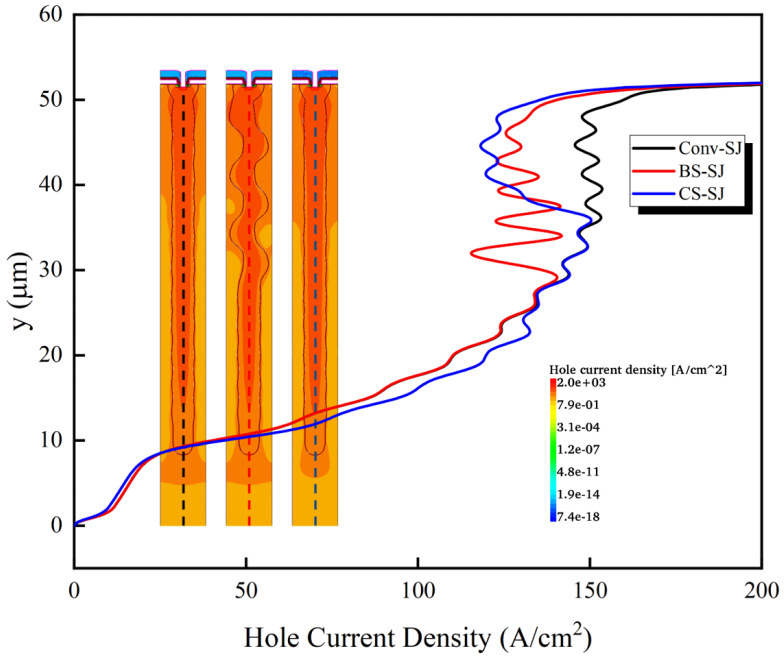

Figure 5. The hole current density along the center (x = 2.75 μm) of the P−pillar when body diode is forward conducting.

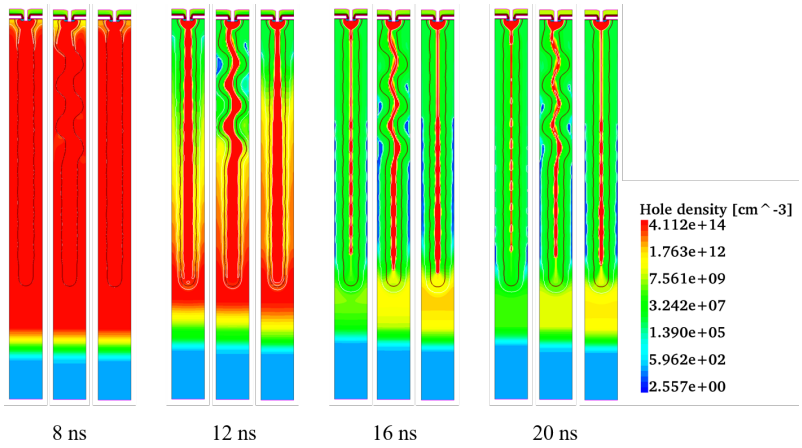

Figure 6. The evolution of the hole density at different time nodes during the reverse recovery carrier sweep out stage of the three devices.

Figure 7 clearly illustrates the variation of the hole carrier concentration over time at the bottom (y = 5 μm) of the three devices during the reverse recovery period. When the reverse recovery reached 8 ns, the hole carrier concentration levels within the Conv-SJ, BS-SJ, and CS-SJ were almost equal, all around the level of 9×10^5 cm^{-3}. However, due to the different sweep out speeds when the reserve recovery reached 12 ns, the concentration difference of residual hole carriers in the three devices became increasingly apparent. After

the reverse recovery progressed to 16 ns, the residual hole carriers concentration of the Conv-SJ was about 2–3 magnitude orders lower than that of the BS-SJ and CS-SJ. This phenomenon indicates that the proposed two novel devices exhibited a longer duration in the hole carrier sweep-out stage, thereby leading to a more gradual and smoother reverse recovery characteristic [16].

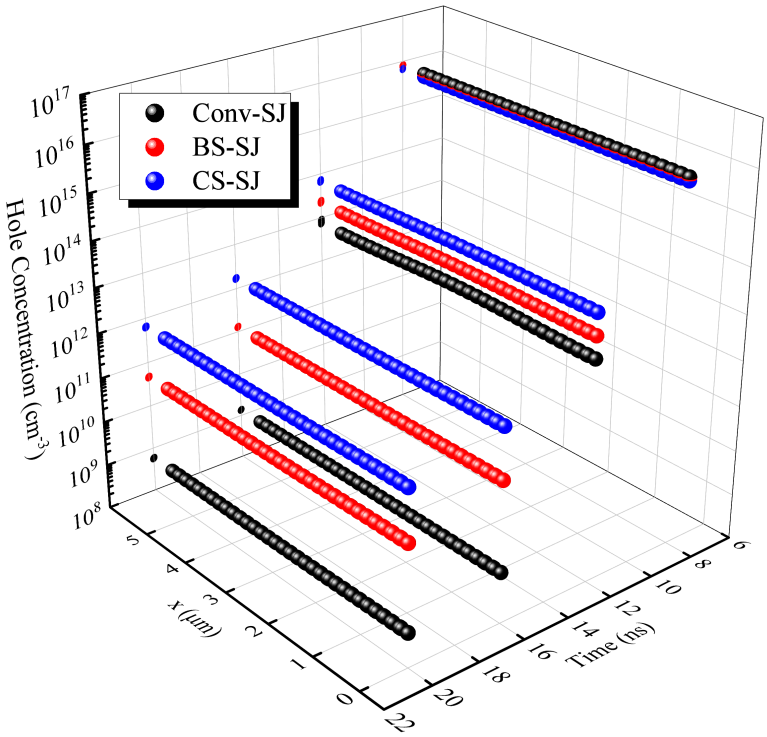

Figure 7. The hole concentration at the bottom (y = 5 μm) of the P-pillar during the reverse recovery carrier sweep-out stage of the three devices.

Figure 8 shows how the reverse recovery waveform varied with the time of the conventional and proposed devices, and the inset illustrates the reverse recovery simulated circuit. This is a typical double-pulse test circuit, with a load inductance (L) set to 200 μH, bus voltage (V_{cc}) set to 100 V, and gate resistance (R_g) set to 10 Ω. The drive switch (DRI) controls the transition process from the forward conduction to the withstand voltage stage of the body diode in the device under test (DUT), where the DUT had an active area of 1.85 mm^2. The reverse recovery peak currents (I_{rrm}) of the 0.7 μm BS-SJ and 35% CS-SJ were 15.23 A and 15.59 A, respectively. These values were 4.9% and 2.8% lower than that of the Conv-SJ (16.04 A). The voltage rising rate (d_v/d_t) of the body diode was markedly reduced from the on state to off state. The d_v/d_t of the 0.7 μm BS-SJ and 35% CS-SJ were 7.1% and 9.3% lower than that of the Conv-SJ, respectively. This reduction in d_v/d_t helps to reduce circuit oscillation. Furthermore, the reverse recovery characteristics of the BCS-SJ, which were created by superposing two doping profile methods, were also studied. The I_{rrm} (14.62 A) and d_v/d_t of the 0.7 μm and 35% BCS-SJ were further reduced to be 8.8% and 13% lower than that of the Conv-SJ, respectively. An important point to consider is that the softness factor S represents the ratio between the carrier extraction time (t_f) and the carrier storage time (t_s) [17]. This factor describes the hardness and softness of the reverse recovery.

Figure 9a,b primarily show the influence of the shift level on I_{rrm} and S, as well as the Q_{rr} and reverse current recovery rate (d_{ir}/d_t), respectively. Compared with the Conv-SJ, the reverse recovery characteristics of the BS-SJ and the CS-SJ were further improved with the increase in the shift level. The d_{ir}/d_t of the 0.7 μm BS-SJ and the 35% CS-SJ were 2176 A/μs and 2228 A/μs, respectively. This represents a 34% and 32% decrease,

respectively, compared to the d_{ir}/d_t value of the Conv-SJ (3299 A/µs). At the same time, at this shift level, the S values of the BS-SJ and CS-SJ were 1.10 and 1.04, respectively. This represents a 64% and 55% increase, respectively, compared to that of the Conv-SJ (0.67). The reason for this is that the shift level was directly correlated with the resistance of the upper half of the P-pillar. Furthermore, when compared to the effect of a single shift factor, the BCS-SJ with two shift factors exhibited superior reverse recovery characteristics at the same shift level. The 0.7 µm and 35% BCS-SJ exhibited d_{ir}/d_t and S values of 1688 A/µs and 1.58, respectively. These values represent a 48% and 135% improvement, respectively, compared to the Conv-SJ. This indicates that the effects of bubble shift and concentration shift on the local resistance of the upper half of the P-pillar were combined.

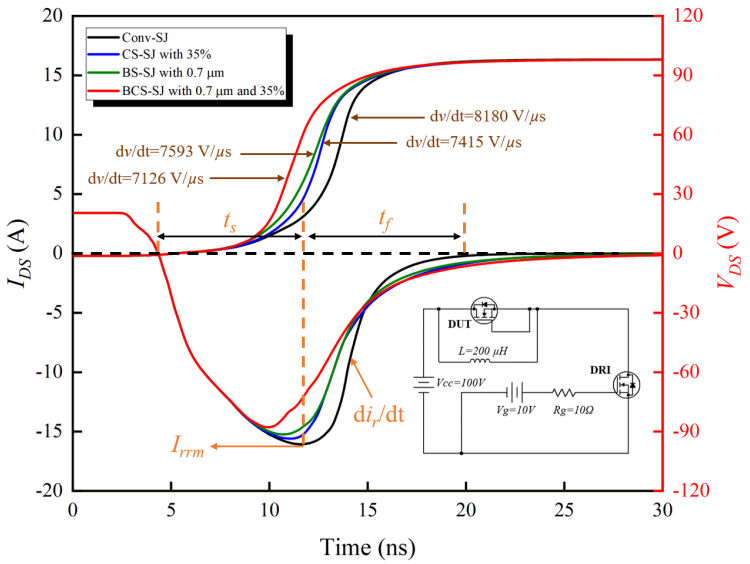

Figure 8. The reverse recovery waveforms of the Conv-SJ, BS-SJ with 0.7 µm bubble shift, CS-SJ with 35% concentration shift, and BCS-SJ with 0.7 µm bubble shift and 35% concentration shift.

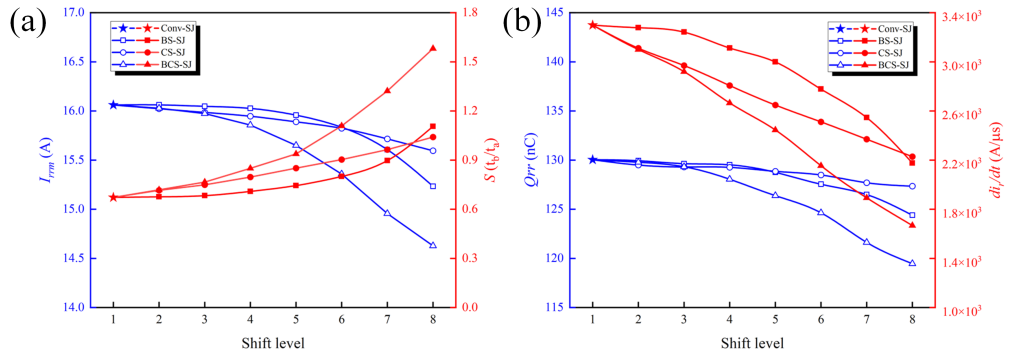

Figure 9. (**a**) The influence of the shift level on the peak reverse recovery current and softness factor. (**b**) The influence of the shift level on the stored charge and reverse current recovery rate.

Polynomial fitting has been used to optimize the field limiting ring (FLR) of SiC JBS devices, which can accurately predict the field limiting ring arrangement and save simulation time [18]. To further explore the synergistic effect of the two doping profile adjustment methods on both dynamic and static characteristics, a polynomial fitting was used to express the trade-off relationship between the BV, R_{on}, and S with respect to the bubble shift and concentration shift. To begin with, the boron bubble shift percentage with respect to the cell pitch (W_c) was defined as ΔB, and the concentration shift percentage of the upper and lower parts of the P-pillar was defined as ΔC. Therefore, the values of ΔB and ΔC determined the shift level for the two doping profiles. Next, we defined the lost

BV, R_{on}, and improved S of the proposed devices as ΔBV, ΔR_{on} and ΔS, respectively, in comparison to the Conv-SJ. After fitting the simulation results of multiple devices with different doping profiles, the following relationship could be obtained.

Figure 10a describes the fitting relationship between the ΔBV, ΔB, and ΔC. The graph shows that the loss of the BV was more sensitive with the concentration shift, and under a high shift level, the BV was entirely determined by the concentration shift. Figure 10b illustrates the fitting surface between the ΔR_{on}, ΔB, and ΔC. In contrast, it is clear that the contributions of the two shift factors to the R_{on} loss were equivalent, and the combined effect of the two doping profiles was more prominent. Meanwhile, Figure 10c describes the relationship between the ΔS, ΔB, and ΔC. In the fitting surface, it is evident that both the bubble shift and concentration shift had a significant optimizing effect on S with increasing shift levels, and their combined effect resulted in an even greater optimizing contribution. Finally, in Figure 10d, the trade-off relationship among the ΔBV, ΔR_{on}, and ΔS based on the proposed doping profile adjustment method is also revealed directly by polynomial fitting.

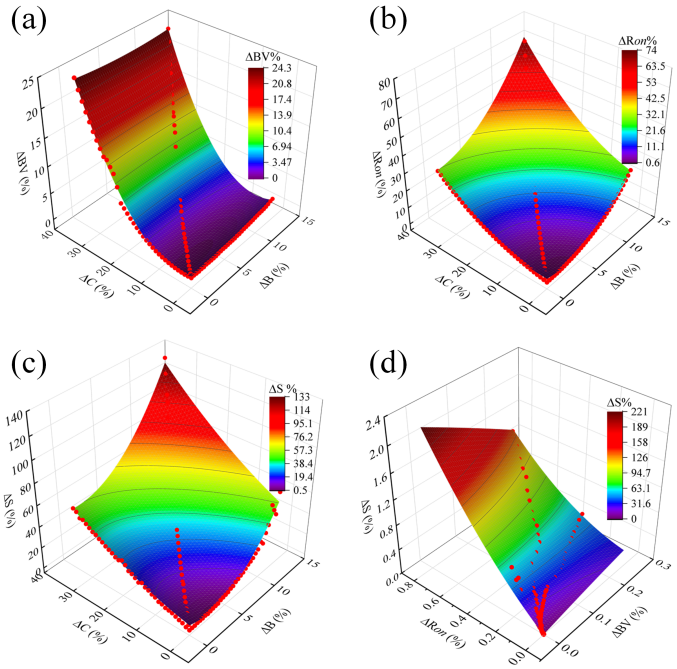

Figure 10. (**a**) The fitting surface of the quadratic function of ΔBV% with respect to ΔB% and ΔC%. (**b**) The fitting surface of the quadratic function of ΔR_{on}% with respect to ΔB% and ΔC%. (**c**) The fitting surface of the quadratic function of ΔS% with respect to ΔB% and ΔC%. (**d**) The fitting surface of the quadratic function of ΔS% with respect to ΔBV% and ΔR_{on}%.

The second-order polynomial fitting relation among the five variables is expressed as:

$$\Delta BV = 1.17 \times \Delta B^2 + 2.57 \times \Delta C^2 - 0.39 \times \Delta B \Delta C - 0.02 \times \Delta B - 0.21 \times \Delta C \quad (1)$$

$$\Delta R_{on} = 24.13 \times \Delta B^2 + 2.43 \times \Delta C^2 + 4.48 \times \Delta B \Delta C - 1.18 \times \Delta B - 0.06 \Delta C + 0.02 \quad (2)$$

$$\Delta S = 54.53 \times \Delta B^2 + 2.05 \times \Delta C^2 + 6.77 \times \Delta B \Delta C - 3.06 \times \Delta B + 0.67 \times \Delta C + 0.05 \quad (3)$$

$$\Delta S = -0.62 \times \Delta BV^2 + 1.15 \times \Delta {R_{on}}^2 - 5.59 \times \Delta BV \Delta R_{on} + 1.28 \times \Delta BV + 1.82 \times \Delta R_{on}. \quad (4)$$

The fitting accuracy improves with an increasing correlation coefficient (R^2). As the R^2 value approaches one, the fitting accuracy further increases. To maintain a balance between the polynomial complexity and the fitting accuracy and to enhance the accuracy of multiple linear regression, a second-order polynomial was chosen for the fitting procedure.

As a consequence, the determination coefficient R^2 for each of these four functions was remarkably high, with values of 0.99, 0.99, 0.97, and 0.99, respectively. These highly accurate formulas enabled the prediction of the BV, R_{on}, and S adjustment amplitudes for various combinations of the two doping profile adjustment methods. This approach provides designers with the flexibility to customize the shift levels according to the specific requirements of diverse application scenarios. As a result, an optimal trade-off can be achieved between the reverse recovery characteristics and the static characteristics of the superjunction MOSFET. This ensures that the device performs satisfactorily and meets the desired performance standards.

4. Conclusions

This paper made two main contributions. Firstly, the bubble-shift SJ (BS-SJ) and concentration shift SJ (CS-SJ) with novel doping profiles were proposed to optimize the reverse recovery characteristics of the parasitic body diodes while sacrificing certain static characteristics. Compared to the conventional SJ (Conv-SJ), the softness factors S of the reverse recovery were improved by 64% and 55%, respectively. Secondly, a measurement method was proposed to balance the dynamic and static characteristics of the superjunction MOSFET under the new doping profiles. These findings provide valuable references for designing high-performance superjunction devices.

Author Contributions: Conceptualization, S.W. and K.L.; methodology, K.L. and S.W.; software, W.Y.; validation, S.L.; formal analysis, X.L.; investigation, K.L. and S.W.; resources, P.F. and H.Y.; data curation, C.T.; writing—original draft preparation, K.L.; writing—review and editing, S.W. and K.L.; visualization, C.T.; supervision, S.W. and H.Y.; project administration, G.Z., funding acquisition, H.Y. All authors have read and agreed to the published version of the manuscript.

Funding: This research was Funded by the Shenzhen Fundamental Research Program (JCYJ20200109140822796).

Institutional Review Board Statement: Not applicable.

Informed Consent Statement: Not applicable.

Data Availability Statement: The data presented in this study are available in the article.

Conflicts of Interest: The authors declare no conflict of interest.

References

1. Li, W.; Huang, H.; Zhang, Z.; Cheng, J.; Yi, B.; Yang, H.; Wang, Z. Optimization of Specific ON-Resistance of Superjunction Device with Two-Zones Variation Vertical Doping Profile. In Proceedings of the 2022 IEEE 16th International Conference on Solid-State & Integrated Circuit Technology (ICSICT), Nanjing, China, 25–28 October 2022; IEEE: Piscataway, NJ, USA, 2022; pp. 1–3.
2. Cheng, C.H.; Huang, C.F.; Lee, K.Y.; Zhao, F. A novel deep junction edge termination for superjunction MOSFETs. *IEEE Electron Device Lett.* **2018**, *39*, 544–547. [CrossRef]
3. Ye, Z.Y.; Liu, L.; Yao, Y.; Lin, M.Z.; Wang, P.F. Fabrication of a 650V superjunction MOSFET with built-in MOS-channel diode for fast reverse recovery. *IEEE Electron Device Lett.* **2019**, *40*, 1159–1162. [CrossRef]
4. Yang, Z.; Zhu, J.; Tong, X.; Sun, W.; Bian, F.; Tian, Y.; Zhu, Y.; Ye, P.; Li, Z.; Hou, B. Investigations of inhomogeneous reverse recovery behavior of the body diode in superjunction MOSFET. In Proceedings of the 2017 29th International Symposium on Power Semiconductor Devices and IC's (ISPSD), Sapporo, Japan, 28 May–1 June 2017; IEEE: Piscataway, NJ, USA, 2017; pp. 155–158.
5. Eikyu, K.; Sakai, A.; Yamashita, T.; Shimomura, A.; Yanagigawa, H.; Mori, K. Multi-trench-gate cell concept for low voltage superjunction power MOSFETs. In Proceedings of the 2020 32nd International Symposium on Power Semiconductor Devices and ICs (ISPSD), Vienna, Austria, 13–18 September 2020; IEEE: Piscataway, NJ, USA, 2020; pp. 553–556.
6. Sharma, S.; Zheng, Y.; Wong, H.Y. Short Circuit Ruggedness of Trench Filled Superjunction Devices. In Proceedings of the 2022 IEEE Latin American Electron Devices Conference (LAEDC), Puebla, Mexico, 4–6 July 2022; IEEE: Piscataway, NJ, USA, 2022; pp. 1–4.
7. Zeng, D.; Zhang, W.; Xiao, S. A high breakdown voltage superjunction mosfet by utilizing double trench filling epitaxy growth. In Proceedings of the 2018 14th IEEE International Conference on Solid-State and Integrated Circuit Technology (ICSICT), Qingdao, China, 31 October–3 November 2018; IEEE: Piscataway, NJ, USA, 2018; pp. 1–3.
8. Lin, Z.; Huang, H.; Chen, X. An improved superjunction structure with variation vertical doping profile. *IEEE Trans. Electron Devices* **2014**, *62*, 228–231. [CrossRef]

9. Chen, H.; Li, X.; Wei, Z.; Sun, C.; Xu, J.; Wang, M. Improved Method to Analysis the Doping Profile for Ion Implants in Silicon. In Proceedings of the 2021 China Semiconductor Technology International Conference (CSTIC), Shanghai, China, 14–15 March 2021; IEEE: Piscataway, NJ, USA, 2021; pp. 1–3.
10. Ren, M.; Li, L.Q.; Lan, Y.; Ma, R.Y.; Zhang, X.; Zheng, F.; Gao, W.; Li, Z.H.; Zhang, B. The Superjunction Device with Optimized Process Window of Breakdown Voltage. In Proceedings of the 2020 IEEE 15th International Conference on Solid-State & Integrated Circuit Technology (ICSICT), Kunming, China, 3–6 November 2020; IEEE: Piscataway, NJ, USA, 2020; pp. 1–3.
11. Huang, M.; Deng, Y.; Lai, L.; Yang, Z.; Gao, B.; Gong, M. A vertical superjunction MOSFET with n-Si and p-3C-SiC pillars. *IEEE Trans. Electron Devices* **2019**, *66*, 3922–3928. [CrossRef]
12. Huang, M.; Li, R.; Yang, Z.; Ma, Y.; Li, Y.; Zhang, X.; Gong, M. A multiepi superjunction MOSFET with a lightly doped MOS-channel diode for improving reverse recovery. *IEEE Trans. Electron Devices* **2021**, *68*, 2401–2407. [CrossRef]
13. Liu, K.; Yuan, W.; Wang, S.; Tan, C.; Ye, H. Study on Reverse Recovery of a P-pillar Tunable Super-Junction MOSFET. In Proceedings of the 2022 23rd International Conference on Electronic Packaging Technology (ICEPT), Dalian, China, 10–13 August 2022; IEEE: Piscataway, NJ, USA, 2022; pp. 1–4.
14. Huang, H.; Hu, K.; Xu, W.; Xu, S.; Cui, W.; Zhang, W.; Ng, W.T. Numerical solutions for electric field lines and breakdown voltages in superjunction-like power devices. *IEEE Trans. Electron Devices* **2020**, *67*, 3898–3902. [CrossRef]
15. Li, R.; Huang, M.; Zhang, X.; Hu, M.; Yang, Z.; Ma, Y.; Gong, M. Superjunction MOSFET with Trench Schottky Contact and Embedded High-k Insulator for Excellent Reverse Recovery. In Proceedings of the 2021 IEEE 14th International Conference on ASIC (ASICON), Kunming, China, 26–29 October 2021; IEEE: Piscataway, NJ, USA, 2021; pp. 1–4.
16. Rajoriya, A.; Shrivastava, M.; Gossner, H.; Schulz, T.; Rao, V.R. Sub 0.5 V operation of performance driven mobile systems based on area scaled tunnel FET devices. *IEEE Trans. Electron Devices* **2013**, *60*, 2626–2633. [CrossRef]
17. Li, P.; Ma, R.; Yang, Z.; Zhang, X.; Wang, D.; Tang, K.; Guo, J.; Hu, S.; Shi, C.; Lin, Z.; et al. Novel Approach Toward Body Diode Reverse Recovery Performance Improvement in Superjunction MOSFETs. *IEEE Electron Device Lett.* **2022**, *43*, 2145–2148. [CrossRef]
18. Tang, M.; Jun, S.; Zhou, Z.; Ge, X.; Liu, D.; Zhou, R. Method of field limiting rings spacing parameter for SiC JBS based on multiple linear regression and polynomial fitting. In Proceedings of the 2020 15th IEEE Conference on Industrial Electronics and Applications (ICIEA), Kristiansand, Norway, 9–13 November 2020; IEEE: Piscataway, NJ, USA, 2020; pp. 1859–1863.